IEEE Access
Multidisciplinary | Rapid Review | Open Access Journal

Received September 23, 2021, accepted October 21, 2021, date of publication October 26, 2021, date of current version October 29, 2021.

Digital Object Identifier 10.1109/ACCESS.2021.3122922

An Advanced Modulation Technique Featuring Neutral Point Voltage Ripple Suppression of Three-Level Converters in High-Speed Drives

CHEN LI, (Student Member, IEEE), TAO YANG, (Senior Member, IEEE), ZHEN HUANG, SEANG SHEN YEOH, SERHIY BOZHKO, (Senior Member, IEEE), AND PATRICK WHEELER, (Fellow, IEEE)

Power Electronics, Machine and Control (PEMC) Research Group, University of Nottingham, Nottingham NG7 2RD, U.K.

Corresponding author: Zhen Huang (zhen.huang@nottingham.ac.uk)

This work was supported by the Clean Sky 2 Joint Undertaking through the European Union's Horizon 2020 Research and Innovation Program under Grant 807081.

ABSTRACT This paper introduces an advanced space vector modulation technique for three-level neutral-point-clamped (3L-NPC) converters. The studied 3L-NPC converters within aircraft electric starter generator (ESG) systems normally operate at high modulation index, low pulse ratio and full power factor range for most of the operation time. Conventional modulation techniques exhibit large neutral point voltage ripple and possible voltage imbalance under such conditions. The increase of neutral point voltage ripple implies significant increase in converter capacitor size and decrease in capacitor reliability. The modulation technique introduced in this paper achieves improved neutral point voltage balancing within each switching period through enhanced applications of small vectors and restriction on medium vectors. The advanced implementation of small vectors is achieved using a sharing factor aided by a robust incremental current prediction procedure. With the predicted machine currents, the proposed method enables the optimum application of small vectors to balance the neutral point voltages. Simulation results based on a PLECS/Simulink model and experimental results obtained from a 45kVA, 32krpm aircraft electric starter generator prototype platform validate the reduction of the neutral point voltage ripple.

INDEX TERMS Aircraft, electric starter generator (ESG), high-speed drive, three-level neutral-point-clamped converter, pulse width modulation, predictive control, state observer.

I. INTRODUCTION

Aircraft electric starter generator (ESG) system represents a key technology within the more electric aircraft (MEA) notion [1]–[5], which has attracted increasing amount of research interest. Several ESG topologies have been reported recently [6]. Popular solutions include three-stage synchronous machine based systems, switch reluctance machine based systems [7] and permanent magnet synchronous machine based system [8]. The permanent magnet synchronous machine (PMSM) based topology is the one showing most potential in terms of size, weight, power density, efficiency and simplicity [9]–[12].

The proposed ESG system operates as an interface between the aircraft engine shaft through a gear box [13] and the aircraft electrical power system. As shown in Figure. 1, the rotor of the PMSM is connected to the engine shaft driven gear box. During the engine starting process, the power electronic converter inverts DC power to AC power and drives the PMSM to accelerate the engine shaft (compressor) up to the ignition speed. After engine ignition and when the engine reaches its self-sustained speed, the ESG will be ready for power generation. In the generation mode, the engine shaft can be treated as large inertia, where mechanical power is extracted and transformed to electric power to supply various onboard electrical loads.

For ESG applications, three-level Neutral Point Clamped (3L-NPC) is chosen over the classic two-level inverter [14] for its advantages in efficiency and performance under a high fundamental frequency [15].

For 3L-NPC converters, the DC-link neutral point voltage imbalance has always been a problem. As imbalance

The associate editor coordinating the review of this manuscript and approving it for publication was Ton Duc Do.

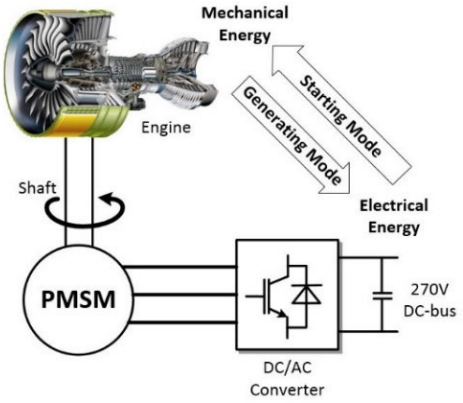

FIGURE 1. PMSM based aircraft electric starter generator system.

of the DC-link capacitor voltages may endanger the capacitor by overvoltage and cause significant output voltage distortion on the AC side. Many methods have been reported in the past, one category being common-mode voltage injection [16]–[19] combined with carrier based pulse width modulation (CPWM). This group of methods inject common-mode voltage by modifying the modulating waveform, so that the average neutral point current is biased towards one direction, achieving neutral point balancing. Alternatively, for 3L-NPC converters with space vector modulation (SVM), the redundancy of the small vectors is exploited to maintain the neutral point balance. As a pair of small vectors with opposite polarities differ in their common-mode voltages, these two methods share some similarities, showing desirable performance under high power factor condition. However, both methods become less effective under reduced power factor condition. There are also harmonic injection methods reported, such as six harmonic voltage injection [20] and even-order current harmonics injection [21].

Apart from neutral point voltage balancing, the 3rd harmonic voltage ripple of the neutral point voltage under high modulation index is another issue that needs to be addressed for its ESG applications [22]. A simpler way is to suppress these harmonics is to increase the capacitance of the capacitor on the dc-link side. However, having large DC-link capacitance would significantly increase the size and weight of the capacitor and thus the converter. This is not desirable for transport related applications especially for MEA applications.

To reduce the 3rd harmonic voltage ripple, a modified space vector modulation technique namely the virtual space vector modulation is proposed [23]. During high modulation index operation, this method ties the duty cycles of two small vectors and the medium vector together, formulating the virtual space vector (VSV). As the virtual space vector connects the DC-link neutral point to all three phases for the same amount of time, the average neutral point current for the virtual vector is zero, thus significantly reducing the 3rd harmonic ripple. However, this method increases the switching loss as well as AC side THDs. Many hybrid modulation techniques are also proposed to achieve a trade-off between the advantages of the conventional SVM method and the virtual SVM method [24], [25]. As the aim of these hybrid solutions is to suppress the 3rd harmonic voltage ripple in the neutral point, the average neutral point current is used to determine whether to use the conventional SVM method or to use VSV based SVM method. The transition process between the two methods have also been improved to achieve a seamless transition with minimum influence on the stability of the control.

As the aircraft starter generator system operates in a wide range of conditions, the performance of the modulation method would have to be optimized for the full operation range. Under light load operation, the power flowing between the machine and the converter is of small amount and therefore a low power factor is expected. High rotation speed of the engine shaft implies the PMSM is constantly operating in flux weakening [26] region with a high fundamental frequency. Therefore, the modulation index for the power converter is constantly near unity. Furthermore, a low pulse ratio is also expected as the switching frequency of the converter is limited. Very few existent SVM techniques can deliver desirable performance under such operating conditions. Furthermore, the extent of the neutral point voltage ripple of 3L-NPC converters directly links to the size of DC-link capacitors and their reliability. Therefore, the modulation technique for 3L-NPC converters in ESG application also needs to minimize the neutral point voltage ripple.

This paper features an improved SVM technique aided by predictive control, aiming at suppression of the neutral point voltage ripple within the entire power factor and modulation index range, to minimize the size of DC-link capacitors whilst improve its reliability. Section II introduces the model of the ESG prototype system as well as its control structure. Section III contains a brief review of operation principles of the 3L-NPC converters and source of the neutral point voltage ripple. The proposed modulation technique and sharing factor calculation are elaborated in section IV followed by simulation results in section V and experimental results from section VI.

II. ESG SYSTEM MODEL & CONTROL

A. ESG MACHINE MODEL

For the studied starter-generator system, a surface-mounted permanent magnet synchronous machine is used. The voltage equations in a synchronous reference frame are presented as follows:

$$V_{abc} = R \cdot I_{abc} + \frac{d\lambda_{abc}}{dt} \tag{1}$$

where resistance matrix R is expressed by:

$$R = \begin{pmatrix} R_s & 0 & 0 \\ 0 & R_s & 0 \\ 0 & 0 & R_s \end{pmatrix} \tag{2}$$

And flux linkage λ_{abc} is expressed by:

$$\lambda_{abc} = L \cdot I_{abc} + \lambda^s_{PM} \tag{3}$$

where inductance matrix L is given as:

$$L = \begin{pmatrix} L_{ls} + L_{ms} & -\frac{1}{2}L_{ms} & -\frac{1}{2}L_{ms} \\ -\frac{1}{2}L_{ms} & L_{ls} + L_{ms} & -\frac{1}{2}L_{ms} \\ -\frac{1}{2}L_{ms} & -\frac{1}{2}L_{ms} & L_{ls} + L_{ms} \end{pmatrix} \tag{4}$$

And permanent magnet flux λ^s_{PM} is:

$$\lambda^s_{PM} = \lambda_{PM} \begin{pmatrix} \sin\theta_r \\ \sin(\theta_r - 2/3\pi) \\ \sin(\theta_r + 2/3\pi) \end{pmatrix} \tag{5}$$

where L_{ls} represents the leakage inductance of stator windings, L_{ms} represents the mutual inductance of stator windings, λ_{PM} represents the permanent magnet flux, and θ_r represents the rotor flux position of the PMSM.

The voltage and flux equations can be transformed from *abc* frame into stationary reference frame using Clarke transformation. The voltage equations in $\alpha\beta$ reference frame is:

$$\begin{aligned} v^s_\alpha &= R_s \cdot i^s_\alpha + \frac{d\lambda^s_\alpha}{dt} \\ v^s_\beta &= R_s \cdot i^s_\beta + \frac{d\lambda^s_\beta}{dt} \end{aligned} \tag{6}$$

And flux linkage being:

$$\begin{aligned} \lambda^s_\alpha &= L_s \cdot i^s_\alpha + \lambda^r_{PM}\cos\theta_r \\ \lambda^s_\beta &= L_s \cdot i^s_\beta + \lambda^r_{PM}\sin\theta_r \end{aligned} \tag{7}$$

Park transformation transforms quantities from $\alpha\beta$ reference frame to synchronous reference frame:

$$\begin{aligned} v^r_d &= R_s \cdot i^r_d - \omega_e\lambda^r_q + \frac{d\lambda^r_d}{dt} \\ v^r_q &= R_s \cdot i^r_q + \omega_e\lambda^r_d + \frac{d\lambda^r_q}{dt} \end{aligned} \tag{8}$$

with

$$\begin{aligned} \lambda^r_d &= L_s i^r_d + \lambda^r_{PM} \\ \lambda^r_q &= L_s i^r_q \end{aligned} \tag{9}$$

B. ESG CONTROL STRUCTURE

The control structure of the ESG system is very close to a vector controlled PMSM drive, where three phase currents are transformed into synchronous reference frame and controlled separately using classic PI controllers with decoupling applied.

In starting mode operation, the ESG system applies a high starting torque to the crank the engine and drives the engine to its ignition speed. As illustrated in Fig. 3, initially the d-axis current reference is zero and the q-axis current reference is set based on a look-up table containing a detailed torque profile of the engine. It should be noted that the required

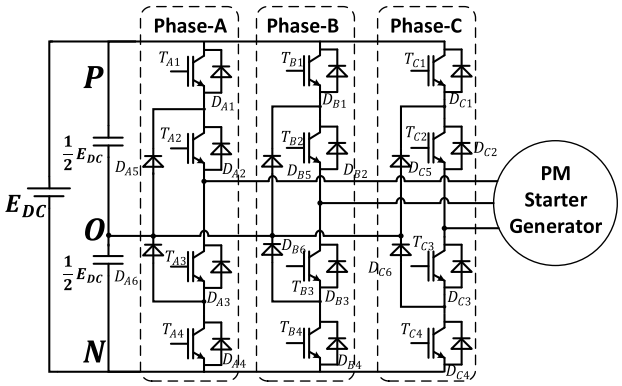

FIGURE 2. Three-level neutral point clamped converter (3L-NPC).

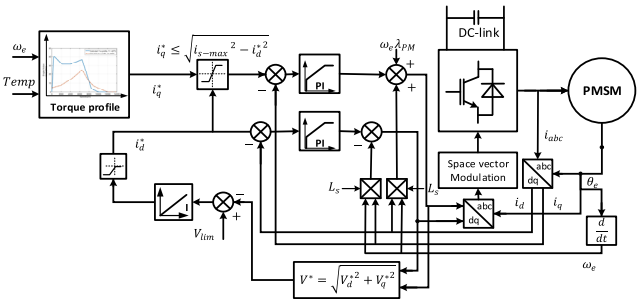

FIGURE 3. ESG control structure in starting mode.

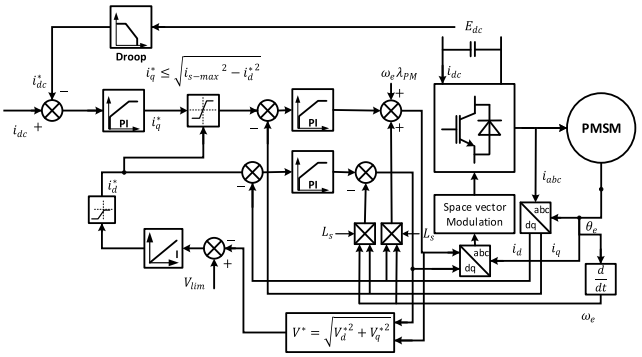

FIGURE 4. ESG control structure in generation mode.

engine starting torque is dependent on its speed as well as the ambient temperature.

After the ESG machine accelerates beyond its base speed, the d-axis current reference will become negative and is generated by integrating the difference between the output voltage reference and converter voltage limit. This also implies that the modulation index of the converter would be near unity after this point of the operation. Furthermore, in flux weakening operation conditions, if overall currents approach the converter current limit (set by thermal limitations), the de-fluxing d-axis current would be given priority whereas the q-axis current reference would be compromised.

In generation mode, the power flows from the engine shaft to the onboard electrical power systems through the ESG systems. As shown in Fig.4, the current regulators as well as the flux weakening controller are remained the same as that in the starting mode. However, the q-axis current reference

TABLE 1. 3L-NPC converter leg switching states.

Phase leg switching state	Switch status x(a/b/c)				Phase leg pole voltage
	T_{x1}	T_{x2}	T_{x3}	T_{x4}	
P	On	On	Off	Off	$E_{DC}/2$
O	Off	On	On	Off	0
N	Off	Off	On	On	$-E_{DC}/2$

is set by a droop controller with the dc-link current reference i^*_{dc} defined by a V-I droop characteristic. The implementation of droop control is for load sharing between multiple parallel ESG systems on a single DC bus [27], [28]. It is worth noting that in this context, the current flowing from the converter to the electrical machine is defined as the positive direction. Therefore, the q-axis current of the PMSM in generating condition is normally negative.

In aircraft operations, some flight scenarios require engines on, but onboard electrical system is not demanding a lot of power from ESG systems. In such condition, the ESG machine would be supplying little amount of active power to the DC-bus, the power flowing between the converter and the machine is mostly reactive. These operation scenarios are defined as light-load or standby conditions. However, as the engine is still spinning at a high speed, the flux-weakening control of the ESG still needs to be active, and a large de-flux current is still required. Therefore, the power converter is operating under high modulation index, low power factor and low sample time ratio condition when the ESG system is under these light-load or standby conditions.

III. NEUTRAL POINT VOLTAGE RIPPLE

A. 3L-NPC OPERATION PRINCIPLE & MODULATION

As illustrated in Fig. 2, the 3L-NPC converter within the prototype ESG systems has three phase legs. Each phase leg can connect the corresponding machine winding to the positive voltage rail of the DC-link (switching state 'P'), DC-link neutral point (switching state 'O') or the negative voltage rail of the DC-link (switching state 'N'). For each 3L-NPC phase leg, each possible switching state and resultant phase leg pole voltages are detailed in Table. 1. Effectively, each 3L-NPC phase leg can be seen as a single pole three throw switch.

Three-level converters offer a total number of 27 different switching vectors with each switching states associated with one switching vector. As shown in Fig. 5, voltage vectors with magnitudes of $\frac{2}{3}V_{DC}$ are large vectors. Voltage vectors which reside at the centre are null vectors. These vectors do not connect any phases to the neutral point. Alternatively, small vectors come in pairs with opposite neutral point current directions. It should be noted in Fig. 5 that each voltage space vector that connects one of the phase winding to the neutral point is marked with its corresponding phase current. With Fig.5a, the neutral point current can be derived from the measured three phase currents and the applied voltage space vector.

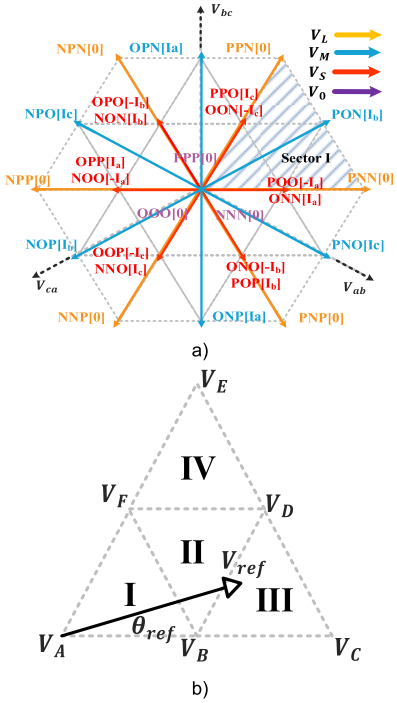

FIGURE 5. 3L-NPC converter operation principle a) space vector diagram b) Conventional SVM technique.

Conventional space vector modulation technique divides the space vector hexagon in Fig. 5(a) into six sectors. Each sector contains four subsectors as shown in Fig. 5(b). The conventional nearest-three-vector space vector modulation (NTV-SVM) method generates the reference vector using its three nearest vectors. Taking the third subsector of the first sector within the space vector hexagon in Fig.5 as an example, the reference vector in subsector III will be synthesized by the three adjacent space vectors, i.e. V_B, V_C and V_D. Duty cycles of these adjacent vectors can be calculated with volt-sec balance principle based on:

$$V_{ref} = d_B V_B + d_C V_C + d_D V_D \tag{10}$$

$$d_B + d_C + d_D = 1 \tag{11}$$

To analyse the neutral point current, this paper assumes a) the DC-link voltage of the 3L-NPC converter is constant; b) the upper and lower capacitors are of the same capacitance; c) the 3L-NPC converter connects to a balanced load, i.e., the surface-mounted permanent magnet synchronous machine in this study. The positive sequence of three phase reference voltages of the converter can be defined as:

$$\begin{aligned} V_a &= m \cdot \left(V_{DC}/\sqrt{3}\right) \cdot \cos\theta \\ V_b &= m \cdot \left(V_{DC}/\sqrt{3}\right) \cdot \cos\left(\theta - 2\pi/3\right) \\ V_c &= m \cdot \left(V_{DC}/\sqrt{3}\right) \cdot \cos\left(\theta + 2\pi/3\right) \end{aligned} \tag{12}$$

where m stands for modulation index and refers to the ratio of the magnitude of the reference voltage vector compared to the maximum voltage in linear modulation area of the space

vector hexagon, i.e. Fundamental components of the three phase currents can be expressed by:

$$\begin{aligned} i_a &= I_s \cdot \cos(\theta - \varphi) \\ i_b &= I_s \cdot \cos(\theta - 2\pi/3 - \varphi) \\ i_c &= I_s \cdot \cos(\theta + 2\pi/3 - \varphi) \end{aligned} \tag{13}$$

where I_s represents the magnitude of the fundamental component of the phase currents, ϕ represents the converter power factor angle.

B. SOURCE OF RIPPLES

With the conventional NTV-SVM, the electron charge flowing into and out of the DC-link neutral point under high modulation index operation can be illustrated by mapping the variation of phase currents and medium vector duty cycles. The charge is represented by a defined variable, current-time-area (ITA). The ITA is defined as

$$ITA = \int_0^{Ts} i_{NP} \cdot dt_{Vm} \tag{14}$$

where i_{NP} is the normalized neutral point current, t_{vm} is the duty cycle of the medium vector, T_s is one switching cycle.

Given a modulation index of 0.8 and a power factor angle of 0.1pi, the variation of medium vector duty cycle and normalized three-phase currents in a fundamental cycle are illustrated in Fig. 6(a). This represents a high modulation index and high-power factor condition as the phase voltages (not shown in the figure) and phase currents are closely aligned. The resultant ITA absorbed by the neutral point caused by the medium vector within one fundamental cycle is given in Fig. 6(b). The way neutral point is connected within a fundamental cycle naturally forms a variation of ITA at three times the fundamental frequency. The average ITA absorbed by the neutral point within a fundamental cycle is zero, therefore under ideal condition the continuous neutral point imbalance will not appear.

The same analysis is also performed at a power factor angle of 0.5pi, the results are presented in Fig. 7. This is referred as a low power factor condition as the three phase voltages (not shown in the figure) and three phase currents become orthogonal. Similarly, the variation of medium vector under such condition reveals a clear variation three times of the fundamental frequency. Comparing the magnitude of the ITA variation between two conditions, it can be observed that the extent of the third harmonic ripple appears at the DC-link neutral point gets significantly increased under low power factor condition.

It is well-established that the manipulation of redundant small vectors can compensate the disturbance to the neutral point voltage caused by the medium vector. Fig. 8 presents a surface plot of the magnitude of the third harmonic ripple appears at the neutral point in full power factor and modulation index range with the compensation capability offered by redundant small vectors been considered. The results show

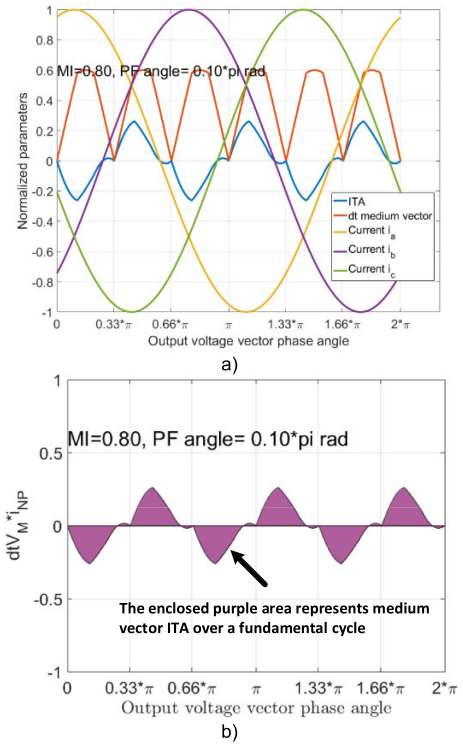

FIGURE 6. Medium vector ITA under high power factor.

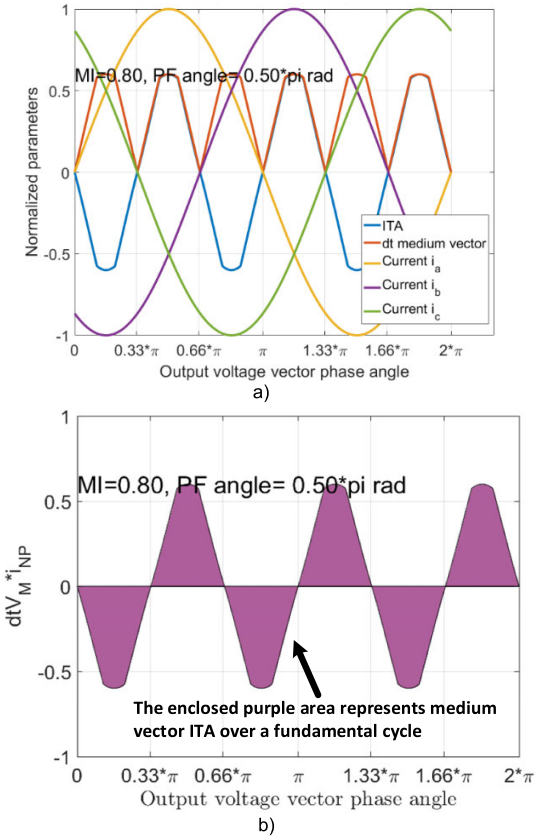

FIGURE 7. Medium vector ITA under low power factor.

that the third harmonic ripple appears at the neutral point is at its peak under high modulation index and low power

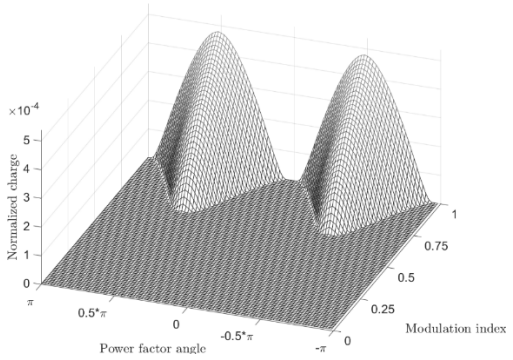

FIGURE 8. 3L-NPC low frequency ripple with respect to modulation index and power factor.

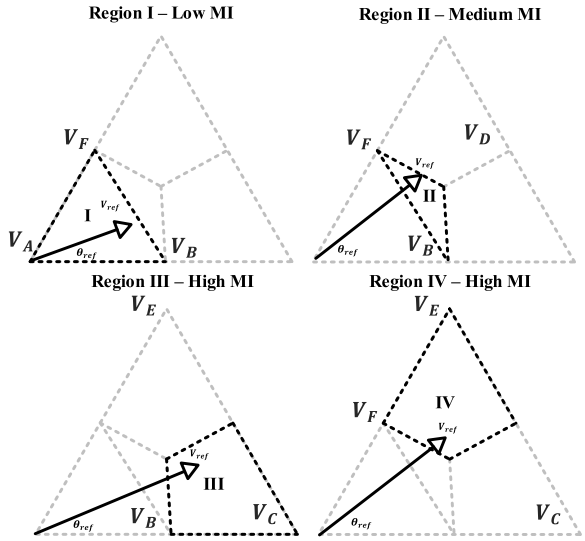

FIGURE 9. Proposed modulation technique – vector selection.

factor condition. Alarmingly, the 3L-NPC converter within the ESG prototype system does operate under such conditions especially under light-load or standby scenarios. To suppress the large low frequency neutral point voltage ripples under such operating conditions, the DC-link capacitance needs to be increased. However, the increase of DC-link capacitance translates into increase of overall size and weight of the 3L-NPC converter, which is undesirable for aircraft starter-generator systems.

IV. PROPOSED MODULATION TECHNIQUE

A. PROPOSED MODULATION METHOD

Presented in Fig. 9, the proposed space vector modulation method selects three voltage space vectors in a switching period and applies them half-wave symmetrically. In low to medium modulation index (MI) region, the principle of voltage space vector selection is the same as NTV-SVM technique. However, to avoid excessive 3rd harmonic voltage ripple in the neutral point, the use of the medium vector is forbidden in high modulation index region, which are subsector III and subsector IV. To replace the medium vector

TABLE 2. Small vector selection table.

ΔV_{DC} \ i_{NP}	$i_{NP} < 0$	$i_{NP} > 0$
$\Delta V_{DC} > 0$	i_{NP} not inverted	i_{NP} inverted
$\Delta V_{DC} < 0$	i_{NP} inverted	i_{NP} not inverted

V_D, a more distant large vector is selected. For subsector III, vector V_E is selected. For subsector IV, vector V_C is selected. For a given voltage space vector magnitude V_{ref} and phase angle θ_{ref}, its subsector can be determined with its indices on gh-axis, duty-cycles can be determined with volt-sec balance principle. Details on subsector determination and duty-cycle calculation can be found in appendix.

B. SMALL VECTOR MANIPULATION

The polarity of the small vector is determined based on the measured neutral point voltage and neutral point current mapped from measured three phase currents. The selection of small vector follows the principle given in Table. 2, where $+i_{NP}$ and $-i_{NP}$ represents the neutral point current remaining the same or being inverted corresponding to the respective small vector. The variable ΔV_{DC} is defined in (15), where V_{Cu} and V_{Cl} represents voltages across the DC-link upper capacitor and the lower capacitor respectively.

$$\Delta V_{DC} = V_{Cu} - V_{Cl} \tag{15}$$

For instance, assuming the reference voltage falls in subsector III in sector I, the voltage space vector selected to synthesize such a reference vector are V_B, V_C and V_E. Among these selected voltage space vectors, selection of the small vector V_B will be determined using Table. 2. Assuming the upper capacitor V_{Cu} has lower voltage than lower capacitor V_{Cl}, i.e. $\Delta V_{DC} < 0$V. According to Fig. 5(a), small vector V_B in sector I corresponds to voltage space vector ONN and POO as in Fig. 10(a) and Fig. 10(b) respectively, both of which connect phase-a to the DC-link neutral point, hence the phase current i_a is the corresponding neutral point current i_{NP}. Assuming the phase current in phase a at this instant is positive, according to Table. 2, voltage vector ONN should be selected given it keeps i_{NP} equal to i_a, whereas POO makes i_{NP} inverted and equals $-i_a$.

Furthermore, typical 1.5 period of sample time delay normally existed in digital controlled motor drives should be compensated before the small vector selection takes place, as such delay has significant impacts on the accuracy of phase currents in terms of zero-crossing. This is especially true for high speed drives. Illustrated in Fig. 11, assuming a very low pulse ratio of 10:1, if the reference voltage vector falls in subsector III in sector I, the small vector V_B will be applied and phase current i_a will be connected to the neutral point. For the $t(k+2)$ instant, the control actions calculated based on i_a at this time instant will be applied 1.5Ts later at $t(k+3.5)$ instant. The polarity of i_a does not change between two instants, therefore would be accurate assuming

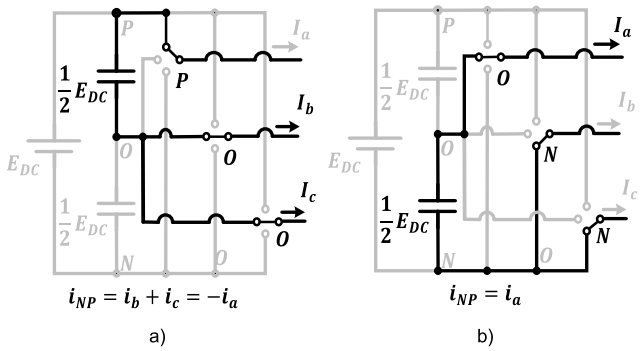

FIGURE 10. Neutral point current paths for switching pattern a) POO and b) ONN.

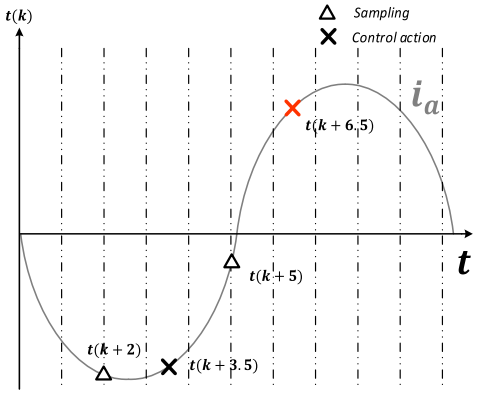

FIGURE 11. Possible phase current zero crossing due to delay.

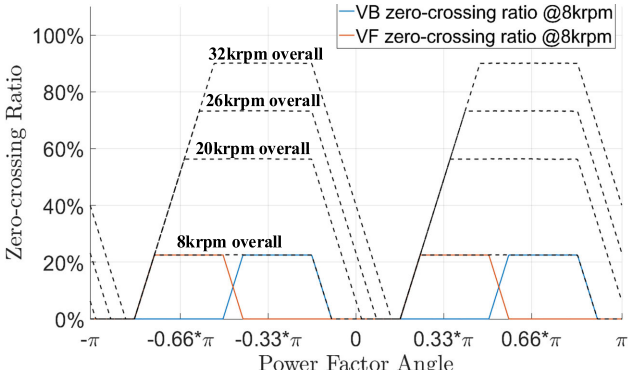

FIGURE 12. Zero-crossing ratio with respect to operating condition.

the change of magnitude of i_a is not considered. However, for the case when the sampling of i_a takes place at instant $t(k+5)$, the corresponding control action happens at instant $t(k+6.5)$. In this case, the phase current i_a is negative at sampling instant but becomes positive when control action is applied. Such zero-crossing phenomenon results in erroneous control action as it is calculated based on the fact that i_a is negative.

For the ESG system in this study, such effect is dependent not only on power factor as in conventional systems, but also highly on the speed of the ESG machine due to its impacts on the fundamental frequency thus the switching ratio. Fig. 12 presents the possibility of small vector phase current zero-crossing due to the 1.5Ts delay (reflected by the zero-crossing ratio, i.e. the zero-cross period over one fundamental cycle) with respect to power factor and machine speed. When the machine is rotating at 8krpm, the possibilities of zero-crossing error for small vector V_B and V_F are mapped with respect to power factor angle separately. Overall zero-crossing ratio for ESG system operating at 8krpm, 20krpm, 26krpm and 32krpm are also mapped with dashed lines. Results show the accuracy of small vector compensation is impaired for more than half of each fundamental electrical cycle, with a magnitude higher than 20%. It is worth noting that when the erroneous small vector is applied, the opposite phase current offsets neutral point balancing capability. Therefore, when the overall zero-crossing ratio is above 50%, it should be assumed that the balancing capability offered by small vectors is completely lost. Furthermore, such effect is worsening with the increase of machine speed, and low power factor region is mostly affected. To address the above-mentioned zero-crossing issue, it is proposed that all sampled phase currents are rotated by $1.5 \cdot \omega_o \cdot T_s$ at the direction rotation before being used in small vector polarity selection procedure as shown in (16),

$$i_{abc}^{corrected} = i_{abc}^{sampled} \cdot e^{-j \cdot 1.5 \cdot \omega_o \cdot T_s} \tag{16}$$

C. POSSIBLE VOLTAGE RIPPLE

With the modulation technique proposed in Section IV.A, the low frequency voltage ripple can be reduced at high modulation index region. Nevertheless, it should be noted that in both region III and region IV, i.e. the high modulation index regions, the selected voltage space vectors are always two large vectors and one adjacent small vector, among which only the small vector affects the neutral point voltage. Therefore, there could be cases where instantaneous neutral point voltage imbalance is increased due to application of one single small vector within one switching cycle.

As illustrated in Fig. 13, similar to the previous section, assuming the reference voltage vector generated by control resides in region III of the first sector as in Fig. 5 and the bottom left condition in Fig. 9, phase-a is connected to the neutral point, therefore the neutral point current equals to phase A current. The condition of neutral point voltage imbalance and polarity of neutral point current dictates the small vector ONN should be chosen to drive the neutral point voltage to a balanced state. However, as the magnitude of voltage imbalance is small, the application of ONN results in a relatively large overshoot and create an even larger neutral point voltage imbalance. This imbalance will remain so till the end of this switching cycle since the large vector has no impact on the neutral point voltage. Given the neutral point voltage is controlled in a hysteresis fashion by the small vector in high modulation index operating condition, such effect would be rampant and only be suppressed in the next switching cycles.

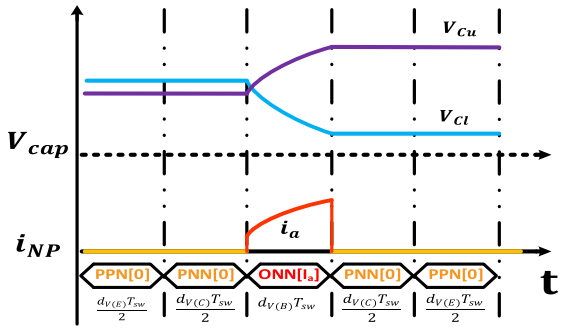

FIGURE 13. Possible downside of the previously proposed method.

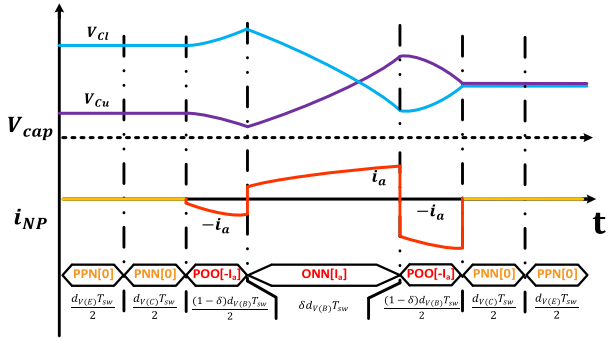

FIGURE 14. Modified space vector modulation method.

D. SHARING FACTOR FOR THE SMALL VECTOR

To address the neutral point voltage overshoot issue illustrated in section IV, a simple solution is to apply the small vector with both polarities. As shown in Fig. 14, the same condition given in Fig. 13 is applied and the same voltage space vectors with the same duty-cycles are selected. However, for the small vector, the two redundant switching patterns (bottom left of Fig. 9) are applied. These two switching states share the duty cycle of the small vector with a sharing factor δ. This will lead to zero neutral point voltage imbalance at the end of the switching period.

The performance of such method is dependent on the accuracy of the sharing factor δ. The charge difference between the upper and the lower DC-link capacitors ΔQ_{NP} under a certain voltage imbalance can be computed as:

$$\Delta Q_{NP} = (V_{Cu} - V_{Cl}) \cdot C_{cap} \tag{17}$$

where C_{cap} represents their capacitance. For the small vector, with its duty-cycle calculated as d_s and neutral point current i_{NP}, the variation of neutral point charge can also be calculated as:

$$\Delta Q_s = d_s T_s \cdot i_{NP} \tag{18}$$

The term T_S is the time of a single switching period. It should be noted that the neutral point current i_{NP} is selected from the phase currents based on information in Fig. 5(a). With existing charge variation ΔQ_{NP} and the future variation of charge ΔQ_S calculated, the sharing factor can then be

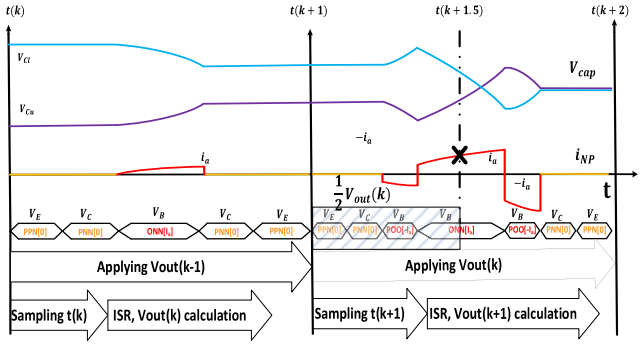

FIGURE 15. Proposed SVM with 1.5 step prediction.

obtained by:

$$\delta = \frac{1}{2}(1 + \frac{\Delta Q_{NP}}{\Delta Q_s}) \tag{19}$$

E. NECESSITY OF DEADBEAT PREDICTION OF PHASE CURRENTS

In most digital controlled systems, the quantities required to compute the control actions are assumed to be remained constant at the sampling instant and the instant when control action is applied. This assumption is not valid under systems with a low pulse ratio such as the ESG system. To address the inaccuracy emerged, section B introduces a phase current correction procedure to compensate possible zero-crossing. However, such method does not consider the variation of the magnitude of phase currents caused by the control actions applied.

To compensate the inaccuracies caused by having a low pulse ratio as well as sampling delay, taking the control actions into account, a 1.5 step prediction method shown in Fig. 15 is introduced to improve the accuracy of the sharing factor. At the time instant $t(k)$, quantities including phase currents, neutral point voltages are sampled, and control action $V_{out}(k-1)$ generated in the previous interrupt service routine (ISR) is applied. As the control action $V_{out}(k-1)$ is known, the quantities at time instant $t(k+1)$ hence the next ISR can be predicted. With the control actions $V_{out}(k)$ generated by executing control algorithm, the average neutral point current for the small vector selected during $t(k+1)$ can be obtained by predicting machine phase currents by 0.5Ts, hence at time instant $t(k+1.5)$. As the voltage space vectors applied is half-wave symmetrical, predicting the quantities at $t(k+1.5)$ from the predicted quantities at $t(k+1)$ can be done by using only half of the output voltage $V_{out}(k)$.

F. ROBUST PHASE CURRENT PREDICTION ALGORITHM

Take the deadbeat prediction of phase current vector i_s from $t(k)$ instant to $t(k+1)$ instant as an example. In the synchronous reference frame, with the voltage and flux equations given in (8) and (9), the discrete form of the PM machine model can be given as:

$$x(k+1) = A(k)x(k) + Bu(k) + d(k) \tag{20}$$

where

$$x(k) = [\, i_d(k) \quad i_q(k) \,]^T, u(k) = [\, u_d(k) \quad u_q(k) \,]^T$$
$$\mathrm{A}(k) = \begin{bmatrix} 1 - {}^{TR_s}/_{L_s} & T\omega_e(k) \\ -T\omega_e(k) & 1 - {}^{TR_s}/_{L_s} \end{bmatrix},$$
$$\mathrm{B}(k) = \begin{bmatrix} {}^{T_s}/_{L_s} & 0 \\ 0 & {}^{T_s}/_{L_s} \end{bmatrix},$$
$$\mathrm{d}(k) = \begin{bmatrix} 0 \\ -{}^{T_s\lambda_{PM}\omega_e(k)}/_{L_s} \end{bmatrix}$$

Within the above-mentioned equation, three machine parameters may affect the accuracy of the predicted phase currents due to parameter variation, which are rotor flux λ_{PM}, stator resistance R_s and stator inductance L_s.

The impact of rotor flux can be eliminated by using an incremental prediction model derived from (20), where:

$$\begin{aligned} \mathrm{x}(k+1) = \mathrm{x}(k) + \mathrm{A}(k)(\mathrm{x}(k) - \mathrm{x}(k-1)) \\ +\mathrm{B}(\mathrm{u}(k) - \mathrm{u}(k-1)) + (\mathrm{d}(k) - \mathrm{d}(k-1)) \end{aligned} \quad (21)$$

Within the equation, the term $(d(k) - d(k-1))$ becomes:

$$\mathrm{d}(k) - \mathrm{d}(k-1) = \begin{bmatrix} 0 \\ -{}^{T_s\lambda_{PM}}/_{L_s}(\omega_e(k) - \omega_e(k-1)) \end{bmatrix} \approx \begin{bmatrix} 0 \\ 0 \end{bmatrix} \quad (22)$$

Furthermore, for the resistance, the term $1 - \frac{TR_s}{L_s}$ in A in (20) yields a result of 0.98 according to the nominal values given in table. 4. Whereas the temperature coefficient for copper is 0.0039 Ω/°C and winding configuration of the ESG machine is made to be slot-per-pole-per-phase $q = 2$, the variation of R_s can be safely ignored.

For stator inductance, variation of d-axis inductance can be ignored since the ESG system is constantly operating in flux-weakening condition and d-axis flux path is not saturated. For q-axis inductance, an extended state observer (ESO) is adopted. The ESO is constructed based on d-axis voltage equation, the model describing the physical system is:

$$\begin{cases} \dot{x}_1 = x_2 + {}^{u_d}/_{L_d} \\ \dot{x}_2 = F \end{cases} \quad (23)$$

where x_1, x_2 are state variables. $x_1 = i_d$, x_2 represents the disturbance which includes the variation of q-axis inductance L_q, F is the rate of change of x_2.

The ESO is constructed as:

$$\begin{cases} \dot{z}_1 = z_2 + {}^{u_d}/_{L_d} + \beta_1(x_1 - z_1) \\ \dot{z}_2 = \beta_2(x_1 - z_1) \end{cases} \quad (24)$$

Subtracting (24) from (23) yields:

$$\begin{aligned} \begin{bmatrix} \dot{x}_1 - \dot{z}_1 \\ \dot{x}_2 - \dot{z}_2 \end{bmatrix} &= \begin{bmatrix} -\beta_1 & 1 \\ -\beta_2 & 0 \end{bmatrix} \begin{bmatrix} x_1 - z_1 \\ x_2 - z_2 \end{bmatrix} + \begin{bmatrix} 0 \\ F \end{bmatrix} \\ &= A_{err} \begin{bmatrix} x_1 - z_1 \\ x_2 - z_2 \end{bmatrix} + d_{err} \end{aligned} \quad (25)$$

Take $e_1 = x_1 - z_1$ and $e_2 = x_2 - z_2$, with proper selection of observer gains β_1 and β_2, z_1 converges to x_1 and z_2 converges to x_2, hence $e_1 \to 0$ and $e_2 \to 0$. Its characteristic equation is given as:

$$c(s) = |sI - A_{err}| = \left| \begin{bmatrix} s + \beta_1 & -1 \\ \beta_2 & 0 \end{bmatrix} \right| = s^2 + \beta_1 s + \beta_2 \quad (26)$$

Its corresponding Routh table:

TABLE 3. ESO routh table.

s^2	1	β_2
s^1	β_1	0

Therefore, as long as both β_1 and β_2 are positive, z_1 will converge to x_1 and z_2 will converge to x_2. In practical application, β_1 is set as $2\omega_{eso}$ and β_2 is set as ω_{eso}^2. ω_{eso} is the bandwidth of the ESO.

The discretized ESO can be obtained by first-order Taylor expansion:

$$\begin{cases} z_1(k+1) = (1 - T_s\beta_1)z_1(k) \\ \quad +T_s(z_2(k) + \beta_2 x_1(k) + {}^{u_d(k)}/_{L_d}) \\ z_2(k+1) = z_2(k) + T_s(x_1(k) - z_1(k)) \end{cases} \quad (27)$$

The term L_q can subsequently be obtained via reforming the expression of z_2:

$$L_q = \frac{L_d z_2(k) + R_s i_d(k)}{\omega_e(k) i_q(k)} \quad (28)$$

Finally, from (21), the incremental prediction model hence the dq-axis currents at $t(k+2)$ instant becomes:

$$\begin{cases} i_d(k+1) = (2 - {}^{TR}/_{L_d})i_d(k) - (1 - {}^{TR}/_{L_d})i_d(k-1) \\ +T\omega[i_q(k) - i_q(k-1)]{}^{L_q}/_{L_d} \\ +{}^{T}/_{L_d}[u_d(k) - u_d(k-1)] \\ i_q(k+1) = (2 - {}^{TR}/_{L_q})i_q(k) - (1 - {}^{TR}/_{L_q})i_q(k-1) \\ -T\omega[i_d(k) - i_d(k-1)]{}^{L_d}/_{L_q} \\ +{}^{T}/_{L_q}[u_q(k) - u_q(k-1)] \end{cases} \quad (29)$$

The dq-axis currents at $t(k+2)$ becomes:

$$\begin{cases} i_d(k+2) = (2 - {}^{TR}/_{L_d})i_d(k+1) - (1 - {}^{TR}/_{L_d})i_d(k) \\ +T\omega[i_q(k+1) - i_q(k)]{}^{L_q}/_{L_d} \\ +{}^{T}/_{L_d}[u_d(k+1) - u_d(k)] \\ i_q(k+2) = (2 - {}^{TR}/_{L_q})i_q(k+1) - (1 - {}^{TR}/_{L_q})i_q(k) \\ -T\omega[i_d(k+1) - i_d(k)]{}^{L_d}/_{L_q} \\ +{}^{T}/_{L_q}[u_q(k+1) - u_q(k)] \end{cases} \quad (30)$$

The dq-axis currents at $t(k+1.5)$ instant can subsequently be obtained as:

$$\begin{cases} i_d(k+1.5) = \dfrac{[i_d(k+2) + i_d(k+1)]}{2} \\ i_q(k+1.5) = \dfrac{[i_q(k+2) + i_q(k+1)]}{2} \end{cases} \quad (31)$$

The rotor flux position variation during sampling period can be compensated by:

$$\theta_r^{k+1.5} = 1.5T_s\omega_r + \theta_r^k \quad (32)$$

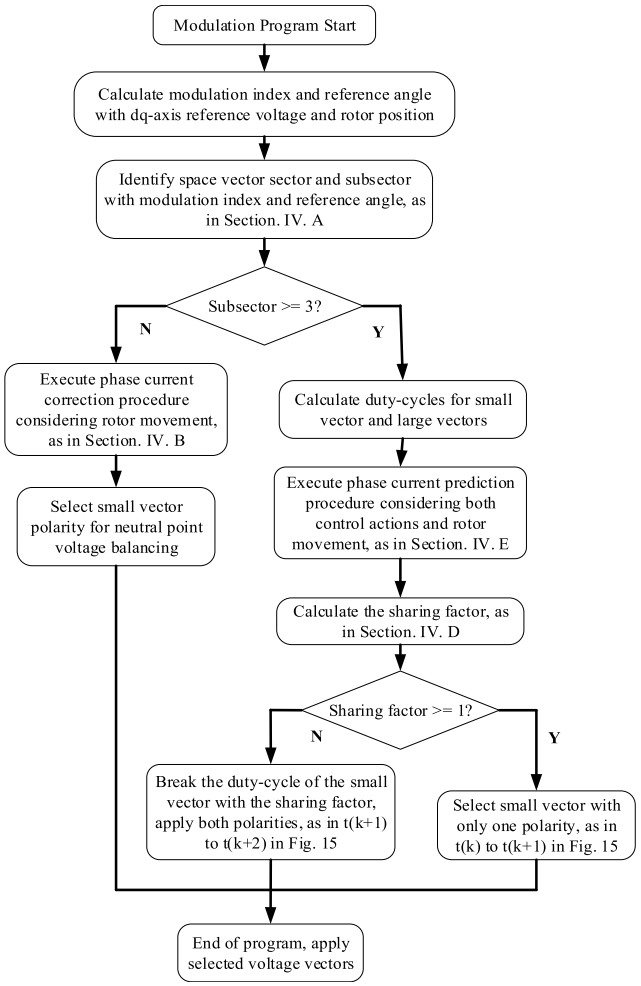

FIGURE 16. Flowchart of the proposed modulation technique.

It is safe to assume that the speed of the ESG stays constant during the sample time delay as mechanical time constant is significantly larger than electrical time constant.

Then, the predicted phase currents at $t(k+1.5)$ instant can be obtained by inverse dq-transformation:

$$i_{abc}^{k+1.5} = \begin{pmatrix} \cos\theta_r^{k+1.5} & -\sin\theta_r^{k+1.5} \\ \cos(\theta_r^{k+1.5} - 2\pi/3) & -\sin(\theta_r^{k+1.5} - 2\pi/3) \\ \cos(\theta_r^{k+1.5} + 2\pi/3) & -\sin(\theta_r^{k+1.5} + 2\pi/3) \end{pmatrix} \times \begin{pmatrix} i_d^{k+1.5} \\ i_q^{k+1.5} \end{pmatrix} \quad (33)$$

G. PROGRAM EXECUTION PROCEDURE

To summarize, a flow-chart for the proposed modulation technique is presented in Fig. 16. Variables including dq-axis output voltage, machine phase currents, machine speed and rotor flux position should have been obtained by sampling and calculation. Initially in the program, the dq-axis output voltage is converted to phase angle and magnitude to determine its sector and subsector. Duty-cycles are calculated as well. If the reference voltage is of low to medium modulation index, hence in subsector I or II, the proposed

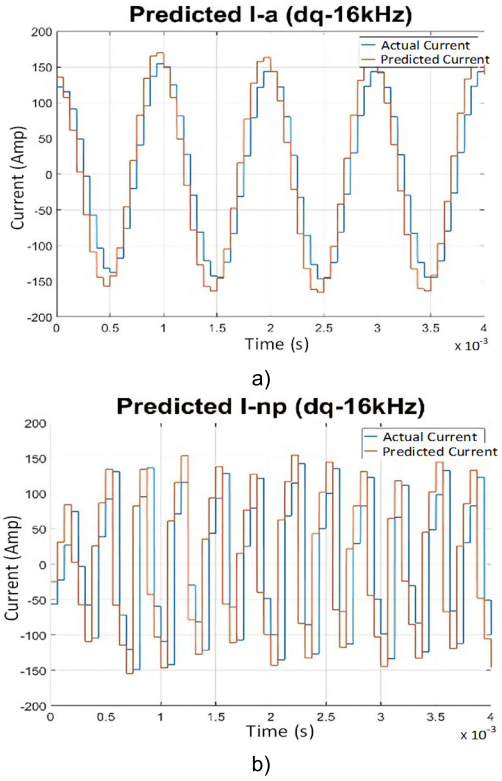

FIGURE 17. Predicted phase current & neutral point current.

modulation technique behaves in a similar fashion as conventional NTV-SVM technique with standard phase current correction applied. In high modulation index region hence subsector III and subsector IV, the phase current deadbeat prediction procedure is applied, followed by the calculation of the sharing factor. If the sharing factor is greater than 1, then there is no need to break the duty-cycle of the small vector. If the sharing factor is lower than 1, the small vector is divided with the sharing factor and applied in a half-wave symmetrical fashion.

V. SIMULATION

Based on the parameters of the prototype ESG test rig given in Table. 4 in the appendix, a simulation model is built with the PLECS/Simulink environment. In simulation, the starting mode operation is not considered as it only accounts for less than 1% of the operation ESG operation time. In generation mode, the ESG machine operates at 20krpm, initially no active power is demanded by the aircraft DC power system, a 20kw resistive load is connected to the DC-link at 1s to simulate an active power demand from the aircraft. Both the conventional NTV-SVM technique and the proposed modulation technique are applied to the 3L-NPC converter. Fig. 17 presents the performance of the prediction mechanism, where Fig. 17(a) shows the measured and the predicted phase-a current, Fig. 17(b) shows the predicted neutral point current.

Fig. 18 presents the ESG machine currents in synchronous reference frame, initially the q-axis current is close to zero as no active power is required, large negative d-axis

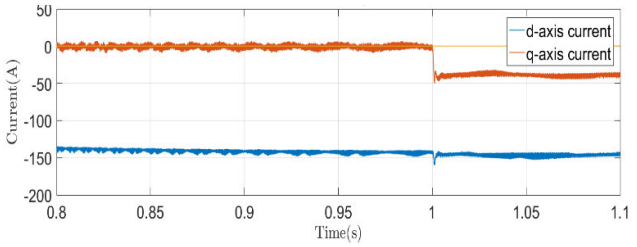

FIGURE 18. ESG machine currents in dq-frame.

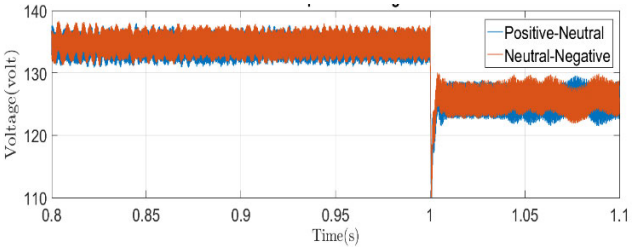

FIGURE 19. DC-link capacitor voltages with NTV-SVM.

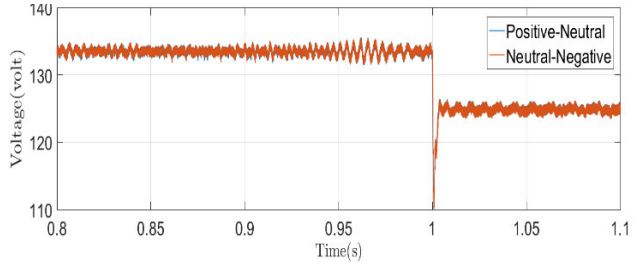

FIGURE 20. DC-link capacitor voltages with the proposed method.

current is constantly required for flux weakening operation. An increase of negative q-axis current is observed when the load is applied. The voltages across DC-link capacitors using the conventional NTV-SVM technique and the proposed technique are presented in Fig. 19 and Fig. 20 respectively. The slight drop of the DC-link capacitor voltages is caused by the droop controller, and the ripple on capacitor voltages is due to high droop gain. Comparing the results from NTV-SVM method and the proposed method, the neutral point voltage ripple is significantly reduced when the proposed method is applied.

VI. EXPERIMENTAL RESULTS

The proposed method is evaluated in a laboratory prototype ESG system capable of 32krpm and 45kVA. As illustrated in Fig. 21, a 150kw prime mover engineered by Torquemeters Ltd along with the ESG machine are in an isolated high-speed test room for safety. A dedicated oil cooling system based Cool-Temp TIL330 is also installed for the ESG machine. Outside the high-speed room, the 3L-NPC converter based on IGBT power modules from Infineon is controlled by DSK6713/Actel A3P400 control platform. The DC-link of the 3L-NPC converter is connected to a grid-connected sink source (GSS) which mimic the 270V aircraft DC-bus. DC-link capacitance is a bespoke module which contains two 600mF film capacitor packed in one unit.

FIGURE 21. The prototype ESG system.

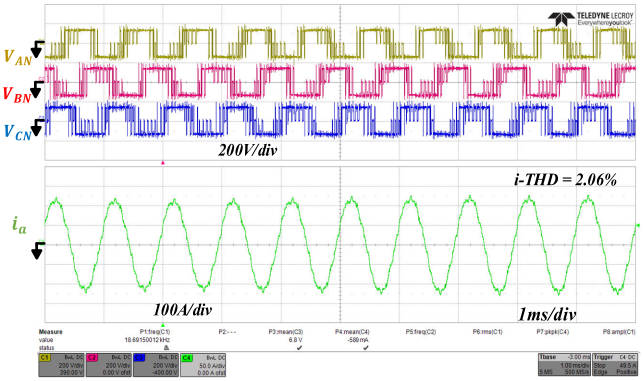

FIGURE 22. Phase voltages and phase current for proposed modulation technique.

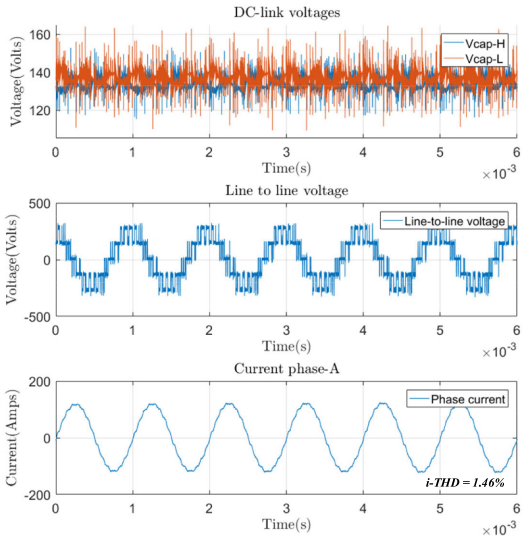

FIGURE 23. NTV-SVM technique in light-load condition.

The proposed modulation technique and the conventional NTV-SVM technique are both evaluated when the ESG system is operating at 20krpm. The ESG system supplies 20kw of active power to the GSS, the q-axis current is approximately -45A. The measured power factor under such condition is 0.57, converter modulation index is constantly

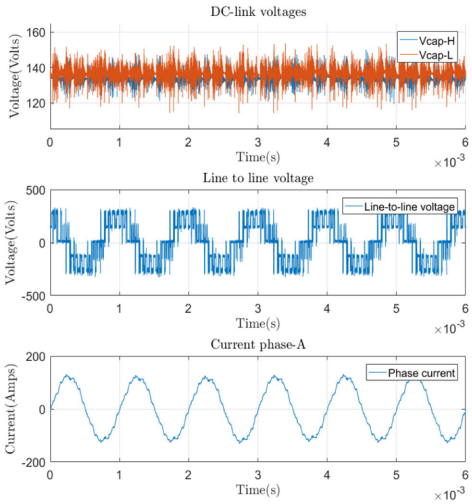

FIGURE 24. Proposed technique in light load condition.

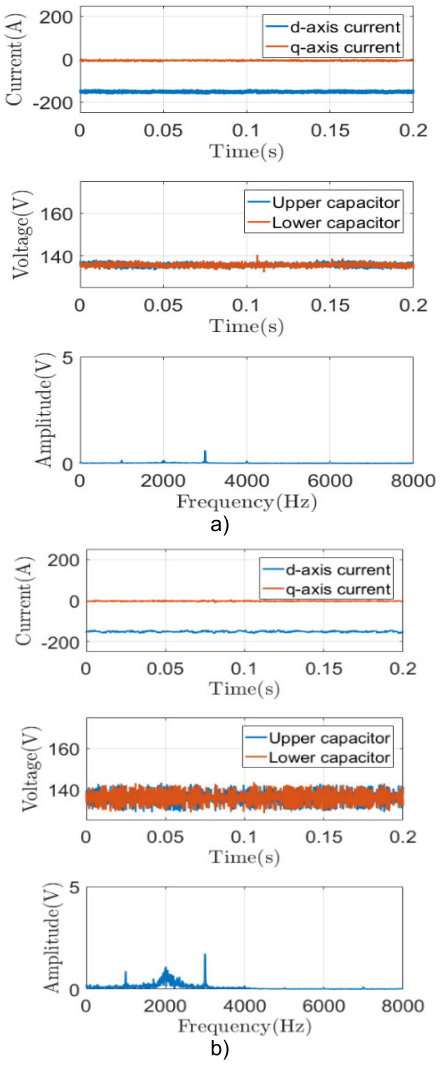

FIGURE 25. Performance comparison in no-load operation.

above 0.9. An oscilloscope screenshot containing phase voltages and phase-a current are presented in Fig. 22.

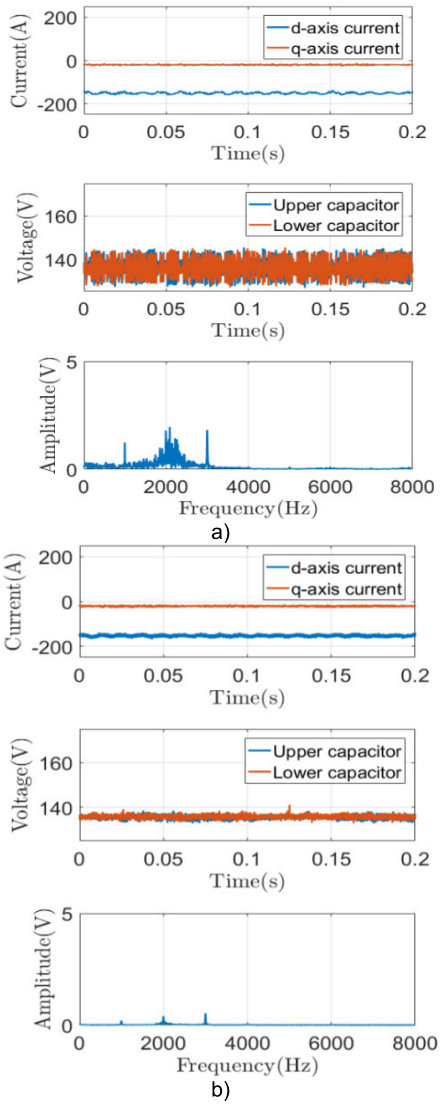

FIGURE 26. Performance comparison at 15kw of active power.

Fig. 23 and Fig. 24 present waveforms of the conventional NTV-SVM technique and the proposed modulation technique. In those two figures, the currents and voltages are measured by their corresponding transducers inside the 3L-NPC converter. The ESG test rig was operating under light-load condition at 20krpm, the active power flowing from the machine to the converter is 3.5kW, the modulation index is above 0.9. Comparing the results, the proposed modulation technique exhibits lower DC-link voltage ripple, even when some high-frequency oscillations were captured by the high-bandwidth scope. On the other hand, the line-to-line voltage indicates a slight increase of switching actions, which leads to a slight increase of switching loss and phase current THD. Measured by PPA5530 power analyzer, the worst-case phase current THD for the proposed method is lower than the 4% dictated by IEEE519 which is for grid applications. Therefore, it is safe to conclude the THD rise caused by the proposed method is acceptable for machine application such as the prototype ESG system used in this study.

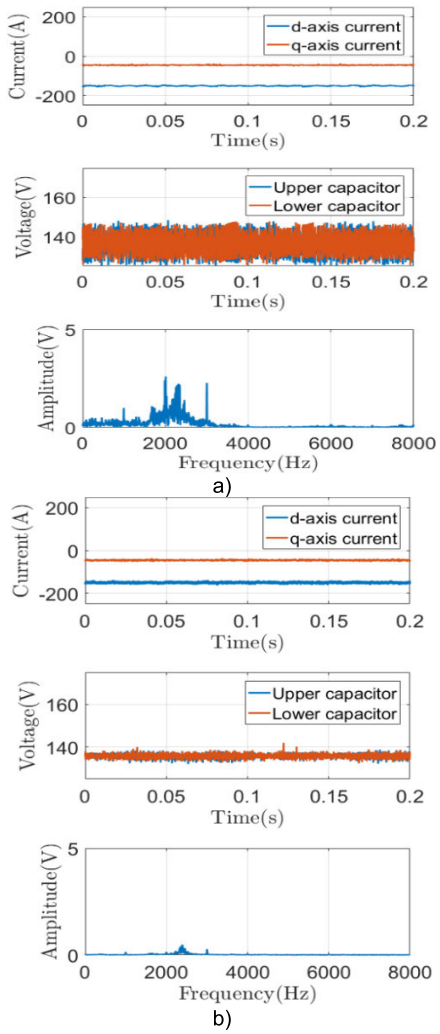

FIGURE 27. Performance comparison at 25kw of active power.

Fig. 25, Fig. 26 and Fig. 27 present comparisons of neutral point voltage ripple caused by the conventional NTV-SVM method and the proposed method under various loading conditions at 20krpm. The results are of lower resolution compared to Fig. 23 and Fig. 24 as they are sampled by DSP platform. Results for the conventional NTV-SVM technique are Fig. 25 (a), Fig. 26 (a) and Fig. 27 (a), results for the proposed method are Fig. 25 (b), Fig. 26 (b) and Fig. 27 (b). With the increase of active power supplied by the ESG system, the neutral point voltage ripple for conventional NTV-SVM method shows a significant increase, such increase is also reflected on the frequency spectrum as evident on the bottom figure in all three figures.

Compared to simulation results illustrated in Fig. 19 and Fig. 20, the neutral point voltage ripple illustrated in Fig. 25 matches with the performance before the load transient in Fig. 19 and Fig. 20. Similarly, the neutral point voltage ripple illustrated in Fig. 26 matches with performances after the loading transient in Fig. 19 and Fig. 20. The voltage ripples in experimental results are larger than that of simulations

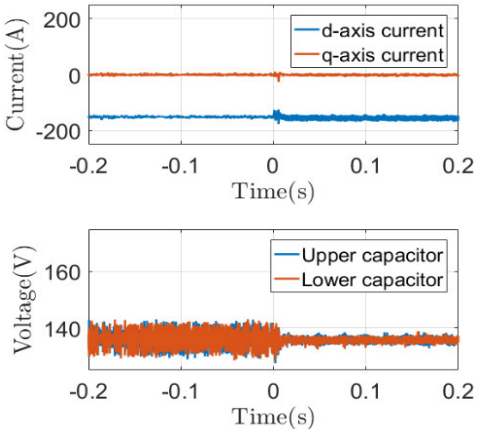

FIGURE 28. Switching from the NTV-SVM technique to the propose modulation technique in no-load condition.

TABLE 4. Starter generator system parameters.

Ld	99uH
Lq	99uH
Is-max	400A
Vdc	270V
PM flux	0.0364 Vs/rad
Pole pair	3
Machine base speed	8000rpm
Converter switching frequency	16kHz
Fundamental frequency in generating	1~1.75kHz

due to surplus voltage ripples induced by converter switching actions.

Fig. 28 presents the transient performance when the ESG system switches from the conventional NTV-SVM method to the proposed method at no-load condition. The increase reduction of DC-link neutral point voltage ripple can be observed more clearly. However, as a downside, it can also be observed that the ripples on dq-axis currents are slightly larger. Similar to Fig. 23 and Fig. 24, this confirms the proposed modulation technique significantly reduces the neutral point voltage ripple at the expense of slightly increasing phase current THD.

VII. CONCLUSION

This paper has addressed a modified space vector modulation technique for three-level neutral point clamped converters within the aircraft electric starter-generator system. The usage of the medium vector is constrained at high modulation index region, leaving only large vectors and small vectors applicable. To reduce the neutral point voltage ripple, both patterns of the selected small vector are utilized with their duty cycles dividing by a sharing factor. A 1.5 step predictive approach is adopted, ensuring the accuracy of that sharing factor. For high-speed drives, a very low pulse ratio of 10:1 can be expected. Under that extreme case, the possible phase current zero-crossing due to delay and the zero-crossing ratio

TABLE 5. Duty cycle calculation.

Region I	$d_B = 2 \cdot M \cdot \sin(\frac{\pi}{3} - \theta_{ref})$ $d_F = 2 \cdot M \cdot \sin(\theta_{ref})$ $d_A = 1 - d_{S0} - d_{S1}$
Region II	$d_B = 1 - 2 \cdot M \cdot \sin(\theta_{ref})$ $d_F = 1 + 2 \cdot M \cdot \sin(\theta_{ref} - \frac{\pi}{3})$ $d_D = 2 \cdot M \cdot \sin\left(\theta_{ref} + \frac{\pi}{3}\right) - 1$
Region III	$d_B = 2 - 2 \cdot M \cdot \sin(\theta_{ref} + \frac{\pi}{3})$ $d_C = \sqrt{3} \cdot \mathrm{M} \cdot \cos(\theta_{ref}) - 1$ $d_E = M \cdot \sin(\theta_{ref})$
Region IV	$d_C = M \cdot \sin(\theta_{ref} - \frac{\pi}{3})$ $d_E = \sqrt{3}\sin(\theta_{ref} + \frac{\pi}{6}) - 1$ $d_F = 2 - 2 \cdot M \cdot \sin(\theta_{ref} + \frac{\pi}{3})$

TABLE 6. Reference voltage subsector determination.

Subsector	Condition for m_g and m_h
I	$m_g + m_h \leq 0.5$
II	$m_g + m_h > 0.5$ && $m_g < 0.5$ && $m_h < 0.5$
III	$m_g > 0.5$ && $m_h > 0.5$ && $m_g \geq m_h$
IV	$m_g > 0.5$ && $m_h > 0.5$ && $m_g < m_h$

with different machine operating conditions were considered. A detailed flowchart of the proposed modulation technique was elaborated, and its robustness was studied. The performance of the proposed method has been validated by the simulation results obtained in a PLECS/Simulink model and experimental results collected from a laboratory ESG system prototype.

APPENDIX

The subsector determination is completed with gh coordinates. For a given voltage space vector, its moduli in gh coordinates can be calculated via (24), and subsector can be subsequently determined with Table. 6.

$$m_g = \sqrt{3}V_{ref} \Big/ V_{DC} \cos\theta_{ref}$$
$$m_h = \sqrt{3}V_{ref} \Big/ V_{DC} \cos({}^{\pi}\!/_{3} - \theta_{ref}) \quad (34)$$

REFERENCES

[1] C. Li, T. Yang, G. Lo Calzo, S. Bozhko, C. Gerada, and P. Wheeler, "An advanced modulation scheme emphasising neutral point ripple suppression using predictive control for three-level NPC converters in aircraft electric starter generator applications," in *Proc. 9th Int. Conf. Power Electron., Mach. Drives (PEMD)*, 2018, pp. 1–7.

[2] C. Li, T. Yang, P. Kulsangcharoen, G. L. Calzo, S. Bozhko, C. Gerada, and P. Wheeler, "A modified neutral point balancing space vector modulation for three-level neutral point clamped converters in high-speed drives," *IEEE Trans. Ind. Electron.*, vol. 66, no. 2, pp. 910–921, Feb. 2019, doi: 10.1109/TIE.2018.2835372.

[3] Z. Huang, T. Yang, J. Adhikari, C. Wang, Z. Wang, S. Bozhko, and P. Wheeler, "Development of high-current solid-state power controllers for aircraft high-voltage DC network applications," *IEEE Access*, vol. 9, pp. 105048–105059, 2021, doi: 10.1109/ACCESS.2021.3099257.

[4] Z. Huang, T. Yang, P. Giangrande, S. Chowdhury, M. Galea, and P. Wheeler, "Enhanced performance of dual inverter with a floating capacitor for motor drive applications," *IEEE Trans. Power Electron.*, vol. 36, no. 6, pp. 6903–6916, Nov. 2020, doi: 10.1109/TPEL.2020.3040029.

[5] Z. Huang, T. Yang, P. Giangrande, M. Galea, and P. Wheeler, "Technical review of dual inverter topologies for more electric aircraft applications," *IEEE Trans. Transport. Electrific.*, early access, Sep. 16, 2021, doi: 10.1109/TTE.2021.3113606.

[6] V. Madonna, P. Giangrande, and M. Galea, "Electrical power generation in aircraft: Review, challenges, and opportunities," *IEEE Trans. Transport. Electrific.*, vol. 4, no. 3, pp. 646–659, Sep. 2018, doi: 10.1109/TTE.2018.2834142.

[7] J. B. Bartolo, M. Degano, J. Espina, and C. Gerada, "Design and initial testing of a high-speed 45-kW switched reluctance drive for aerospace application," *IEEE Trans. Ind. Electron.*, vol. 64, no. 2, pp. 988–997, Feb. 2017, doi: 10.1109/TIE.2016.2618342.

[8] Z. Huang, T. Yang, P. Giangrande, S. Chowdhury, M. Galea, and P. Wheeler, "An active modulation scheme to boost voltage utilization of the dual converter with a floating bridge," *IEEE Trans. Ind. Electron.*, vol. 66, no. 7, pp. 5623–5633, Jul. 2019, doi: 10.1109/TIE.2018.2873539.

[9] D. Golovanov, L. Papini, D. Gerada, Z. Xu, and C. Gerada, "Multidomain optimization of high-power-density PM electrical machines for system architecture selection," *IEEE Trans. Ind. Electron.*, vol. 65, no. 7, pp. 5302–5312, Jul. 2018, doi: 10.1109/TIE.2017.2772188.

[10] F. Zhang, D. Gerada, Z. Xu, X. Zhang, C. Tighe, H. Zhang, and C. Gerada, "Back-iron extension thermal benefits for electrical machines with concentrated windings," *IEEE Trans. Ind. Electron.*, vol. 67, no. 3, pp. 1728–1738, Mar. 2020, doi: 10.1109/TIE.2019.2903758.

[11] X. Lang, T. Yang, Z. Huang, C. Wang, Z. Wang, S. Bozhko, and P. Wheeler, "Stability improvement of onboard HVDC grid and engine using an advanced power generation center for the more-electric aircraft," *IEEE Trans. Transport. Electrific.*, early access, Jul. 7, 2021, doi: 10.1109/TTE.2021.3095256.

[12] C. Wang, T. Yang, H. Hussaini, Z. Huang, and S. Bozhko, "Power quality improvement using an active power sharing scheme in more electric aircraft," *IEEE Trans. Ind. Electron.*, early access, May 4, 2021, doi: 10.1109/TIE.2021.3076401.

[13] N. Chai, M. Yang, Q. Ni, and D. Xu, "Gear fault diagnosis based on dual parameter optimized resonance-based sparse signal decomposition of motor current," *IEEE Trans. Ind. Appl.*, vol. 54, no. 4, pp. 3782–3792, Jul. 2018, doi: 10.1109/TIA.2018.2821099.

[14] F. Guo, T. Yang, C. Li, S. Bozhko, and P. Wheeler, "Active modulation strategy for capacitor voltage balancing of three-level neutral-point-clamped converters in high-speed drives," *IEEE Trans. Ind. Electron.*, early access, Mar. 17, 2021, doi: 10.1109/TIE.2021.3065605.

[15] F. Guo, T. Yang, A. M. Diab, S. S. Yeoh, C. Li, S. Bozhko, and P. Wheeler, "An overmodulation algorithm with neutral-point voltage balancing for three-level converters in high-speed aerospace drives," *IEEE Trans. Power Electron.*, vol. 37, no. 2, pp. 2021–2032, Feb. 2022, doi: 10.1109/TPEL.2021.3105752.

[16] M. Schweizer, T. Friedli, and J. Kolar, "Comparative evaluation of advanced 3-phase 3-level inverter/converter topologies against 2-level systems," *IEEE Trans. Ind. Electron.*, vol. 60, no. 12, pp. 5515–5527, Dec. 2013, doi: 10.1109/TIE.2012.2233698.

[17] Y. Zhang, J. Li, X. Li, Y. Cao, M. Sumner, and C. Xia, "A method for the suppression of fluctuations in the neutral-point potential of a three-level NPC inverter with a capacitor-voltage loop," *IEEE Trans. Power Electron.*, vol. 32, no. 1, pp. 825–836, Jan. 2017, doi: 10.1109/TPEL.2016.2536176.

[18] C. Wang and Y. Li, "Analysis and calculation of zero-sequence voltage considering neutral-point potential balancing in three-level NPC converters," *IEEE Trans. Ind. Electron.*, vol. 57, no. 7, pp. 2262–2271, Jul. 2010, doi: 10.1109/TIE.2009.2024093.

[19] C. Newton and M. Sumner, "Neutral point control for multi-level inverters: Theory, design and operational limitations," in *Proc. IEEE Ind. Appl. Conf. 32nd IAS Annu. Meeting*, vol. 2, Oct. 1997, pp. 1336–1343, doi: 10.1109/IAS.1997.629031.

[20] H. Akagi and T. Hatada, "Voltage balancing control for a three-level diode-clamped converter in a medium-voltage transformerless hybrid active filter," *IEEE Trans. Power Electron.*, vol. 24, no. 3, pp. 571–579, Mar. 2009, doi: 10.1109/TPEL.2009.2012528.

[21] M. Marchesoni, P. Segarich, and E. Soressi, "A new control strategy for neutral-point-clamped active rectifiers," *IEEE Trans. Ind. Electron.*, vol. 52, no. 2, pp. 462–470, Apr. 2005, doi: 10.1109/TIE.2005.843909.
[22] N. Celanovic and D. Boroyevich, "A comprehensive study of neutral-point voltage balancing problem in three-level neutral-point-clamped voltage source PWM inverters," *IEEE Trans. Power Electron.*, vol. 15, no. 2, pp. 242–249, Mar. 2000, doi: 10.1109/63.838096.
[23] C. Xia, H. Shao, Y. Zhang, and X. He, "Adjustable proportional hybrid SVPWM strategy for neutral-point-clamped three-level inverters," *IEEE Trans. Ind. Electron.*, vol. 60, no. 10, pp. 4234–4242, Oct. 2013, doi: 10.1109/TIE.2012.2213558.
[24] G. I. Orfanoudakis, M. A. Yuratich, and S. M. Sharkh, "Nearest-vector modulation strategies with minimum amplitude of low-frequency neutral-point voltage oscillations for the neutral-point-clamped converter," *IEEE Trans. Power Electron.*, vol. 28, no. 10, pp. 4485–4499, Oct. 2013, doi: 10.1109/TPEL.2012.2236686.
[25] A. Choudhury, P. Pillay, and S. S. Williamson, "DC-bus voltage balancing algorithm for three-level neutral-point-clamped (NPC) traction inverter drive with modified virtual space vector," *IEEE Trans. Ind. Appl.*, vol. 52, no. 5, pp. 3958–3967, Sep. 2016, doi: 10.1109/TIA.2016.2566600.
[26] Y. Chen, X. Huang, J. Wang, F. Niu, J. Zhang, Y. Fang, and L. Wu, "Improved flux-weakening control of IPMSMs based on torque feed-forward technique," *IEEE Trans. Power Electron.*, vol. 33, no. 12, pp. 10970–10978, Dec. 2018, doi: 10.1109/TPEL.2018.2810862.
[27] F. Gao, S. Bozhko, A. Costabeber, C. Patel, P. Wheeler, C. I. Hill, and G. Asher, "Comparative stability analysis of droop control approaches in voltage-source-converter-based DC microgrids," *IEEE Trans. Power Electron.*, vol. 32, no. 3, pp. 2395–2415, Mar. 2017, doi: 10.1109/TPEL.2016.2567780.
[28] F. Gao, S. Bozhko, A. Costabeber, G. Asher, and P. Wheeler, "Control design and voltage stability analysis of a droop-controlled electrical power system for more electric aircraft," *IEEE Trans. Ind. Electron.*, vol. 64, no. 12, pp. 9271–9281, Dec. 2017, doi: 10.1109/TIE.2017.2711552.

CHEN LI (Student Member, IEEE) received the B.Eng. and Ph.D. degrees in electrical and electronics engineering from the University of Nottingham, Nottingham, U.K., in 2016 and 2021, respectively.

His research interests include high-speed drives, aerospace power electronic converters, more electric aircrafts, and sensorless control of ac drives. He was a recipient of the Outstanding Paper Award for IEEE TRANSACTIONS ON INDUSTRIAL ELECTRONICS 2020.

TAO YANG (Senior Member, IEEE) received the Ph.D. degree in electrical engineering from the University of Nottingham, U.K., in 2013.

Since 2013, he has been a Researcher with the Power Electronics, Machines and Control Group, University of Nottingham, where he became an Assistant Professor, in 2016, and an Associate Professor, in 2019. His research interests include high-speed electric motor drive control, power electronic conversion, and electrical system design and optimization for more electric/hybrid/all-electric aircraft applications.

Dr. Yang is an Associate Editor of the IEEE TRANSACTIONS ON TRANSPORTATION ELECTRIFICATION and *Chinese Journal of Aeronautics*.

ZHEN HUANG received the B.Eng. degree (Hons.) in electrical and electronics engineering and the Ph.D. degree in electrical engineering from the University of Nottingham, Nottingham, U.K., in 2015 and 2019, respectively.

Since January 2020, he has been a Research Fellow with the Power Electronics, Machines and Control Group, University of Nottingham. His research interests include high-speed machine drives, multilevel converters, and on-board electrical power system protection for hybrid/all-electric vehicles and more/all-electric aircraft applications.

SEANG SHEN YEOH received the M.Sc. degree (Hons.) in power electronics and the Ph.D. degree in electrical engineering from the University of Nottingham, U.K., in 2011 and 2016, respectively. Since then, he has been a Research Fellow with the Power Electronics, Machines, and Controls Research Group, University of Nottingham. His current research interests include aircraft power systems, namely modeling and stability studies of complex power systems, and new control strategies for high-speed drive systems.

SERHIY BOZHKO (Senior Member, IEEE) received the M.Sc. and Ph.D. degrees in electromechanical systems from the National Technical University of Ukraine, Kyiv City, Ukraine, in 1987 and 1994, respectively.

Since 2000, he has been with the Power Electronics, Machines and Controls Research Group, University of Nottingham, U.K., where he is currently a Professor of aircraft electric power systems and the Director of the Institute for Aerospace Technology. He is leading several EU- and industry funded projects in the area of aircraft electric power systems, including power generation, distribution and conversion, power quality, control and stability issues, power management and optimization, as well as advanced modeling and simulations methods.

PATRICK WHEELER (Fellow, IEEE) received the B.Eng. degree (Hons.) in electrical engineering and the Ph.D. degree for his work on matrix converters from the University of Bristol, Bristol, U.K., in 1990 and 1994, respectively.

In 1993, he moved to the University of Nottingham, Nottingham, U.K., and worked as a Research Assistant with the Department of Electrical and Electronic Engineering. In 1996, he became a Lecturer with the Power Electronics, Machines and Control Group, University of Nottingham, where he has been a Full Professor, since January 2008. From 2015 to 2018, he was the Head of the Department of Electrical and Electronic Engineering, University of Nottingham. From 2016 to 2020, he was the Li Dak Sum Chair Professor in Electrical and Aerospace Engineering. He is currently the Head of the Power Electronics, Machines and Control Research Group and the Global Director of the Institute of Aerospace Technology, University of Nottingham. He has authored/coauthored over 700 academic publications in leading international conferences and journals.

Prof. Wheeler is a member of the IEEE PELS AdCom. From 2013 to 2017, he was an IEEE PELS Distinguished Lecturer.